PAPER

Check for updates

Toward rational design of TADF two-coordinate coinage metal complexes: understanding the relationship between natural transition orbital overlap and photophysical properties†

Tian-yi Li,[ab] Jonas Schaab,[a] Peter I. Djurovich [ID][a] and Mark E. Thompson [ID] *[a]

A series of twelve two-coordinate coinage metal, Cu, Ag and Au, complexes with carbene-metal-amide structures were prepared. The complexes all display thermal assisted delayed fluorescence (TADF) emission at room temperature from interligand charge transfer (ICT) excited state with short lifetimes (less than 2 μs) and photoluminescent quantum yields that reach near unity. Owing to the involvement of the substituents in the emissive transitions and different metal ion volume, the natural transition orbital (NTO) overlap of the emissive state can be adjusted in a wide range from 0.21 to 0.41. Investigations on the relationship between the NTO overlap of the emissive state and key TADF photophysical properties demonstrated that both singlet–triplet energy gap and radiative decay rate of S_1 state increase along with the NTO overlap exponentially. Consequently, the overall TADF radiative decay rate leads to a maximum when plotted against the NTO overlap, giving the ideal zone from 0.25 to 0.30 for high TADF radiative decay rate in this class of two-coordinate coinage metal complex luminophores.

Introduction

Thermally assisted delayed fluorescence (TADF), also known as E-type delayed fluorescence, has been investigated in a wide range of photophysical and photochemical applications.[1–11] The process involves the endothermic intersystem crossing (ISC) from the triplet excited state (T_1) to singlet (S_1) excited state followed by emission from the S_1 state (Scheme 1).[12] A recent promising application of TADF emitters is to replace heavy-metal (Ir, Pt and Rh *etc.*) phosphorescent complexes used as luminescent dopants in commercial organic light emitting- diodes (OLEDs).[13] Both TADF and heavy-metal phosphors provide a means to achieve near 100% efficiency in these devices.[14–17] Organic TADF luminophores adopt donor-acceptor (D–A) structure with large dihedral angle between the D–A moieties.[18] Such a twisted geometry leads to weak coupling between D and A, and thus a small energy gap between the S_1 and T_1 states

(ΔE_{ST}), favoring thermal activation from the triplet to the singlet state at room temperature.

Three- and four-coordinate Cu(I) complexes have also been reported that demonstrate TADF behavior, from largely metal to ligand charge transfer (MLCT) transitions.[19–24] Recently, a significant advance in Cu(I)-based TADF materials was achieved using two-coordinate complexes with a carbene ligand to serve as an acceptor and an amide ligand as a donor.[25–36] In addition to the copper complexes, isoelectronic silver and gold based complexes have been shown to give highly efficient TADF.[31,36–38] Here we will refer to the (carbene)M(amide) family of complexes as cMa for M = Cu(I), Ag(I) and Au(I). Early reports of complexes with cMa structures and their promising luminescent properties[39] led to further study[40–42] and successful application in OLEDs generated new enthusiasm for these types of emitters.[25,28–30,37] Investigations have been carried out focusing on two-coordinate TADF complexes experimentally and theoretically, to develop structure–property relationships and strategies to achieve high radiative (k_r) and low non-radiative (k_{nr}) decay rates.[29–31,38,43–48]

TADF molecules fall into two basic categories, depending on whether they have slow or fast rates for intersystem crossing (ISC).[12] Organic TADF materials generally have slow ISC rates ($k_{ISC} = 10^5–10^8$ s^{-1}) owing to weak spin-orbital coupling (SOC), which makes fluorescent radiative decay ($k_r^{S_1}$) competitive with intersystem crossing.[49] Consequently, the radiative decay rate for TADF (k_r^{TADF}) is intimately tied to k_{ISC} (both $S_1 \rightarrow T_1$ and $T_1 \rightarrow S_1$) and the

[a] Department of Chemistry, University of Southern California, Los Angeles, CA, USA. E-mail: met@usc.edu

[b] School of Chemistry and Biological Engineering, Department of Physical Chemistry, University of Science and Technology Beijing, Beijing, 100083, China

† Electronic supplementary information (ESI) available: Experimental details, crystallographic data, calculation results, complete photophysical characteristics and analysis. The *.xyz files are given for the geometry optimized structures. CCDC 2117673, 2117674, 2117675 and 2117672. For ESI and crystallographic data in CIF or other electronic format see DOI: 10.1039/d2tc00163b

4674 | *J. Mater. Chem. C*, 2022, **10**, 4674–4683

This journal is © The Royal Society of Chemistry 2022

Scheme 1 The kinetic scheme for emission *via* TADF mechanism in two-coordinate coinage metal complex, where $k_r^{S_1}$ and k_r^{TADF} are radiative decay rates of S_1 state and TADF process, K_{eq} indicates the equilibrium constant between S_1 and T_1 states *via* ISC transitions.

radiative rate of S_1 $\left(k_r^{S_1}\right)$. In contrast, cMa complexes have ISC rates that are markedly faster ($k_{ISC} = 10^{10}$–10^{11} s^{-1}) than $k_r^{S_1}$ owing to high SOC imparted by the central metal ion.[31] Such rapid rates for k_{ISC} means the equilibrium between singlet and triplet excited states is established rapidly, well before the emission from S_1. Compounds where than ISC rate exceeds $k_r^{S_1}$ allow one to employ the pre-equilibrium approximation such that the equilibrium constant (K_{eq}) becomes a principal factor that determines k_r^{TADF} as shown in eqn (1):[12]

$$k_r^{TADF} = k_r^{S_1} \Delta K_{eq} (T_1 \rightleftharpoons S_1) \tag{1}$$

In this equation, k_r^{TADF} is dependent on $k_r^{S_1}$ and K_{eq}, the latter which is related to ΔE_{ST}. Thus, it is not necessary to know the exact ISC rates in these cMa emitters provided they are faster than $k_r^{S_1}$. The pronounced differences in ISC rates of organic *versus* cMa TADF emitters result in characteristic transient decay behavior from the excited state. Luminescence decay traces from organic TADF emitters typically display a short lived "prompt" fluorescence (ns time scale) and a longer lived "delayed" fluorescence (usually >1 μs, even up to ms timescale).[18] The prompt signal is a combination of radiative fluorescence from the S_1 state and nonradiative ISC to the triplet state, where the delayed k_r^{TADF} is controlled by ISC back to the S_1 state ($T_1 \rightarrow S_1$). However, the absence of a "prompt" process is often manifested in the cMa emitters since equilibration between the S_1 and T_1 states is typically faster than the instrument response function of the detector (on the order of less than 200 ps).[31] Consequently, the emissive decay traces of cMa molecules is usually observed as a single exponential signal on μs scale, similar to those seen in phosphorescent complexes.

According to the analysis above, predictions can be made regarding the TADF properties of cMa complexes without prior knowledge about ISC rates since only $k_r^{S_1}$ and ΔE_{ST} need to be determined to determine k_r^{TADF}. The values of $k_r^{S_1}$ can be obtained experimentally from absorption spectra according to

the Strickler–Berg equation, whereas fits of temperature dependent luminescence data can be used to accurately derive ΔE_{ST} values. In this contribution, we explore the use of the spatial overlap between the hole and electron natural transition orbitals (NTOs) to predict k_r^{TADF} in cMa emitters. The value of the NTO overlap can range from zero—which indicates purely CT transitions with no spatial overlap—to unity where excitation is localized on the same molecular orbital. The use of NTO overlap to predict TADF properties has been reported; however, this analysis only considered the impact of NTO overlap on the magnitude of ΔE_{ST}.[50] Although a small ΔE_{ST} will give rise to more efficient ISC for $T_1 \rightarrow S_1$, a small NTO overlap also results in a low oscillator strength for emission from the S_1 state, and thus a lower $k_r^{S_1}$ which is detrimental for k_r^{TADF}. As the value for NTO overlap influences both variables critical for k_r^{TADF}, but with countervailing effects, a question is raised: is there an optimal value of NTO overlap where the two parameters are ideal? Here, by investigating a large family of cMa complexes with NTO overlaps ranging from 0.2 to 0.4, together with insight into their photophysical parameters, an optimal region for high k_r^{TADF} in cMa complexes were identified to be from 0.25 to 0.30. Such analysis was also applied for organic TADF emitters, providing useful trends for these materials as well.

Results and discussion

The general synthetic route to the compounds studied here is presented in Fig. 1, detailed synthetic procedures and characterization are included in the (ESI†). The N-heterocyclic carbene (NHC) precursor triflate salts **2** were prepared according to a published Ag(I) catalyzed 6-endo-dig cyclization.[51] The diisopropyl phenyl (dipp) substituents on the carbene nitrogen atoms hinder axial rotation around the metal–ligand bonds.[29,38] The preparation of the intermediate complex **3** varied depending on the metal ions. For Cu complexes, deprotonation of **2** with strong base provided the free carbene *in situ*, and the products were obtained by reacting it with CuCl. For Ag complexes, **2** was treated with Ag$_2$O and the triflate salt was isolated. The Au chloride complexes were synthesized *via* a metal exchange reaction with the Ag triflate salts using chloro-dimethylsulfide-gold$^{(I)}$. The cMa complexes were then prepared by reacting **3** with deprotonated carbazole or 3-cyanocarbazole, in yields over 70%. All these complexes were obtained as light yellow to orange crystalline powders. No obvious decomposition is observed in the ^{1}H NMR spectra when the complexes are

Fig. 1 General synthetic route for the coinage metal complexes, note, the counter ion for **3** is triflate in Ag complex.

This journal is © The Royal Society of Chemistry 2022

J. Mater. Chem. C, 2022, **10**, 4674–4683 | **4675**

stored under ambient conditions. Acronyms to distinguish the complexes are given as R_1–**M** or R_1–M^{CN}, where R_1 is Me (methyl) or Ph (phenyl) according to the substituent group, **M** is Cu, Ag or Au and the superscript CN is shown when R_2 is CN.

Molecular structures for five of the complexes were determined using single crystal X-ray analysis. Critical crystallographic data and molecular structures of **Me–Cu** and **Ph–Au^C** are shown in Fig. 2. As revealed by the diffraction results, the molecules present linear two-coordination geometry with near coplanar orientation of NHC and carbazole ligands in agreement with data from analogous cMa derivatives.[29–31,48] The dihedral angles between the two ligands planes range from $0.3°$ to $12.7°$. The C_{NHC}–M bond is longer than the M–N_{Cz} bond in **Me–Cu**, but they become near equal in **Me–Ag**. In Au complexes, the C_{NHC}–Au is shorter than the M–N_{Cz}. The $C_{NHC} \cdots N_{Cz}$ distances in these complexes agree with our previous observations in related (carbene)M(amide) complexes Cu ($\sim$3.7 Å) < Au ($\sim$4.0 Å) < Ag ($\sim$4.1 Å).[31] Metal–metal contacts are all > 8 Å and π–π contacts are well outside of van der Waals contacts in the packing of these complexes in the solid state. Packing diagrams are given in the ESI.†

The electrochemical properties of the complexes were investigated using cyclic voltammetry (CV) and differential pulsed voltammetry (DPV) methods (see ESI† for the electrochemical traces and data). All the complexes undergo irreversible oxidation in DMF solution. For complexes with same ligands, the metal ion influenced E_{ox} in a sequence of Ag < Cu < Au in steps of 0.1 V. Upon introduction of CN on the Cz ligand, the oxidation potential (E_{ox}) positively shifted by 0.24–0.29 V. A single reversible reduction ($E_{red} = -2.25$ to -2.37 V) is observed for complexes with methyl substituted carbenes within the measurable solvent window. Complexes with phenyl substituted carbenes show two reversible reductions, a reversible reduction near -2.0 V and an irreversible reduction at roughly -2.6 V. It is noteworthy that variations in E_{red} between complexes with the same ligands and different metal ions are relatively small, i.e., the range for Cu, Ag and Au complexes is 0.07 V.

The photophysical properties of the two-coordinate complexes were studied in fluid solution and in doped polystyrene (PS) films. The absorption and emission spectra in the two media are very similar, however, determining an extinction coefficient in a polymer thin film is problematic, so here we show toluene solutions for absorbance. Polystyrene is the preferred medium for photoluminescence as it prevents ligand rotation that can lead to nonradiative decay. Other than a difference in extinction coefficients between the three metals (vide infra) the absorption and emission spectra for Cu, Ag and Au complexes with identical ligands show very similar profiles. Representative spectra for the Cu derivatives are shown in Fig. 3, spectra for the Ag and Au derivatives are given in the ESI† and data for all complexes is tabulated in Table 1. UV-visible absorption spectra for the copper-based complexes (Fig. 3(a)) show π–π^* transitions of the carbene ligands below 300 nm, transitions on the Cz ligands appear as well-structured bands from 300 to 375 nm and the broad, featureless bands at lowest energy are assigned to ICT transitions (Cz → carbene). Introduction of the CN substituent on Cz ligand stabilizes the HOMO and leads to a blue shift of 20 nm in the ICT absorption band. Replacing the methyl group with phenyl in the carbene ligand destabilizes the LUMO and leads to a further blue shift of roughly 15 nm. The effect of both substituents increases the energy of the ICT transition, resulting in blue shifted $S_0 \rightarrow S_1$ absorption bands. The principal difference between the complexes imparted by the three metal ions is that the extinction coefficients for the ICT transitions fall in the order Au > Cu > Ag. This trend can be rationalized as reflecting the effects of an extensive polarizability of the Au complexes and the large separation between the donor (carbazolyl) and acceptor (carbene) ligands in Ag complexes, with the Cu derivative falling between those two extremes.

The cMa complexes all display a broad visible ICT emission band when doped in a PS film at room temperature (Fig. 3(b)). The emission energies are principally controlled by substituents on the ligands; changes in the metal ion lead to only minor shifts in energy. The introduction of the CN substituent on Cz ligand induces a hypsochromic shift of around 50 nm.
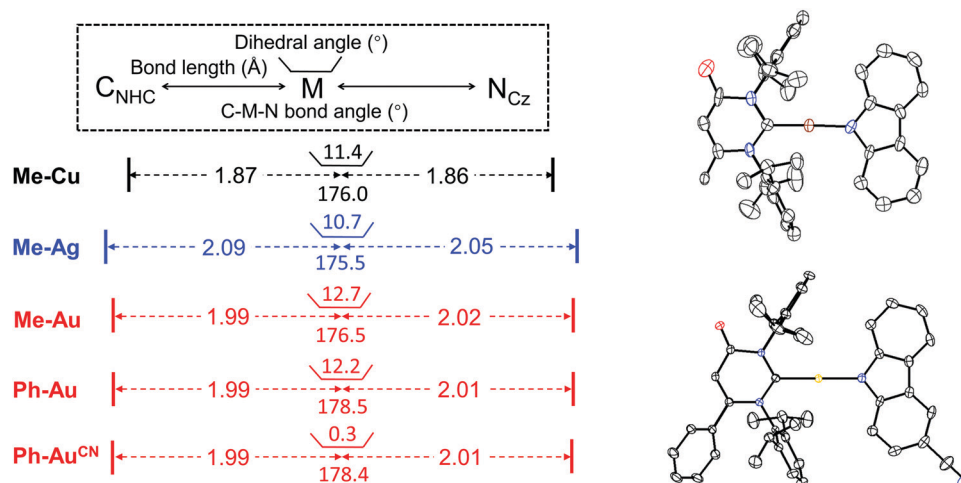

Fig. 2 Critical crystallographic data from X-ray single crystal diffraction measurements, C_{NHC} denotes the carbene carbon and N_{Cz} is the carbazolyl nitrogen. Thermal ellipsoid figures of **Me–Cu** (top) and **Ph–Au^{CN}** (bottom).

4676 | J. Mater. Chem. C, 2022, **10**, 4674–4683

This journal is © The Royal Society of Chemistry 2022

Fig. 3 (a) Absorption and (b) emission spectra of Cu-based complexes. Absorption spectra recorded in toluene solution at room temperature and emission spectra in doped PS (1 wt%) films at room temperature (solid) and 77 K (dash).

Table 1 Photophysical properties of the cMa complexes at room temperature[a]

Complex	$\lambda_{\max}^{abs}$ (nm)	ε (M^{-1} cm^{-1})	$\lambda_{\max}^{em}$ (nm)	Φ_{PL}	τ (μs)	k_r (× 10^6 s^{-1})	k_{nr} (× 10^6 s^{-1})
Me–Cu^{CN}	413	6300	482	0.77	1.4	0.55	0.16
Ph–Cu^{CN}	427	5460	500	0.83	1.1	0.75	0.15
Me–Cu	449	5470	534	0.58	1.5	0.39	0.28
Ph–Cu	468	4820	556	0.70	0.97	0.72	0.31
Me–Ag^{CN}	398	1990	476	0.83	0.41	2.0	0.41
Ph–Ag^{CN}	412	2120	498	0.88	0.60	1.5	0.20
Me–Ag	438	1960	530	0.77	0.41	1.9	0.56
Ph–Ag	456	2070	558	0.56	0.53	1.1	0.83
Me–Au^{CN}	409	8670	484	0.50	0.81	0.62	0.62
Ph–Au^{CN}	421	8330	504	1.00	0.82	1.2	<0.01
Me–Au	442	8180	528	0.50	1.1	0.45	0.45
Ph–Au	459	7550	554	0.77	0.80	0.96	0.29

[a] Absorption data recorded in toluene solution, luminescence data in doped PS (1 wt%) films.

Complexes with the phenyl substituted carbene are red shifted by 25 nm from the methyl substituted analogs. These shifts can be explained by stabilization of the HOMO and LUMO, respectively, in analogy to shifts in the corresponding ICT absorption transitions. The complexes are all highly efficient luminophores ($\Phi_{PL} \geq 0.5$) with short emission lifetimes. The high Φ_{PL} values are a consequence of radiative decay rates on the order of 10^5 to 10^6 s^{-1}. The radiative decay rates for complexes with CN substituted Cz are faster than the analogues with Cz ligand, consistent with their blue shifted emission. Nearly all the complexes retain broad ICT emission profiles at 77 K in PS film (**Me–Ag^{CN}** is the only one that gives structured emission at 77 K). The luminescence lifetimes become substantially longer upon cooling, with larger changes observed for the Cu (τ = 93–256 μs) and Au (τ = 47–82 μs) derivatives than for the Ag complexes (τ = 2.7–7.2 μs). The large increase in decay lifetimes is comparable to changes found in related two-coordinated cMa derivatives and consistent with TADF phenomenon being responsible for luminescence in these compounds.

As discussed in the Introduction, the rate of emission is controlled by $k_r^{S_1}$ and ΔE_{ST} in TADF luminophores that have fast ISC rates (where S$_1$ is the ^{1}ICT state for cMa complexes discussed in this paper). In a study of related cMa complexes it was shown that both parameters could be accurately determined from fits to the temperature dependent luminescent decay rates between 200 and 300 °C. The kinetic scheme employed to fit the temperature dependent lifetime data uses a modified Arrhenius type equation (eqn (2)).[31] The slope of this fit gives ΔE_{ST} whereas the intercept provides $k_r^{S_1}$. For this fit to be valid the zero-field splitting of the triplet sublevels (ZFS) must be $\ll \Delta E_{ST}$ to ensure that the emission in the 200–300 °C range is due solely to TADF and that temperature dependent phosphorescence is not contributing to the decay rate. This is a valid assumption for cMa complexes.[34] Fits for the methyl-substituted carbene complexes are shown in Fig. 4 (fits for the phenyl-substituted carbazole complexes are given in the ESI†) and the values for ΔE_{ST} are given in Table 2.

$$\ln\left(k_r^{TADF}\right) = \ln\left(\frac{k_{ISC}^{S_1 \to T_1}}{3}\left(1 - \frac{k_{ISC}^{S_1 \to T_1}}{k_r^{S_1} + k_{ISC}^{S_1 \to T_1}}\right)\right) - \frac{\Delta E_{ST}}{k_B T}$$
$$= \ln(b) - \frac{1}{T}\left(\frac{\Delta E_{ST}}{k_B}\right) \qquad (2)$$

In our previous studies of related cMa complexes values for $k_r^{S_1}$ were determined from the intercept of linear fits to eqn (3); however, this approach was for samples where nonradiative

This journal is © The Royal Society of Chemistry 2022

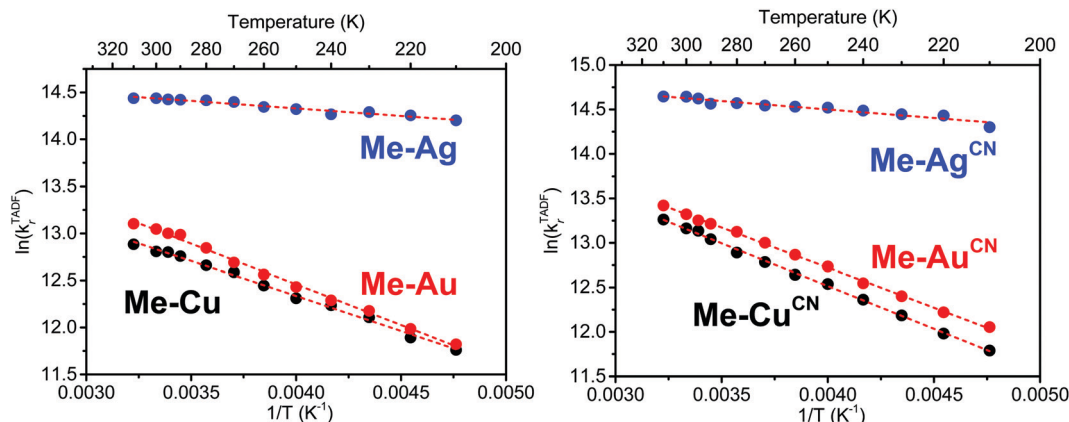*J. Mater. Chem. C*, 2022, **10**, 4674–4683 | **4677**

Fig. 4 Fits to the temperature dependent TADF radiative decay rate from 210 to 310 K according to the full kinetic dynamic scheme.

Table 2 TADF related photophysical data and calculated NTO overlap values

Complex	Cpd. no.	k_r^{TADF} (10^6 s^{-1})	k_r^{TADF}/E^3 (10^4 s^{-1} eV^{-3})	ΔE_{ST} (meV)	$k_{r,kT}^{S_1}$ (10^6 s^{-1})	$k_{r,SB}^{S_1}$ (10^6 s^{-1})	NTO overlap (S_1)	NTO overlap (T_1)
Me–Cu^{CN}	1	0.55	3.1	83	38	34	0.361	0.456
Ph–Cu^{CN}	2	0.75	4.8	55	19	25	0.301	0.433
Me–Cu	3	0.39	3.0	64	13	24	0.377	0.450
Ph–Cu	4	0.72	6.5	55	19	18	0.311	0.418
Me–Ag^{CN}	5	2.0	11	16	13	14	0.272	0.360
Ph–Ag^{CN}	6	1.5	9.5	10	6.7	15	0.211	0.309
Me–Ag	7	1.9	15	14	9.5	11	0.268	0.343
Ph–Ag	8	1.1	9.6	14	5.5	11	0.212	0.289
Me–Au^{CN}	9	0.62	3.6	78	37	46	0.391	0.509
Ph–Au^{CN}	10	1.2	8.2	61	38	39	0.364	0.498
Me–Au	11	0.45	3.6	75	25	37	0.411	0.500
Ph–Au	12	0.96	8.6	59	28	29	0.342	0.477

decay was slow and temperature independent ($\Phi_{PL} \sim 1$).[31] Although some of the samples here have $\Phi_{PL} \sim 1$, others are markedly below this value. Therefore, to correct for any temperature dependence of $k_{nr}^{S_1}$, k_r^{TADF} was calculated from the PL efficiency determined at each temperature (see ESI†) and those values were used to estimate $k_r^{S_1}$ from fits to eqn (2). Alternately, a method for estimating $k_r^{S_1}$ described by Strickler and Berg can be used based on the absorption spectra.[52,53] This analysis uses the integrated extinction spectrum for the ^{1}ICT band to estimate the oscillator strength and Einstein equation to give the radiative rate (see ESI† for details). To evaluate both methods for determining $k_r^{S_1}$, radiative rates from the temperature dependent studies $\left(k_{r,kT}^{S_1}\right)$ were compared to estimates for $k_r^{S_1}$ from a Strickler–Berg analysis of the absorption spectra in toluene solution $\left(k_{r,SB}^{S_1}\right)$. The relationship between the two values was plotted (Fig. S25, ESI†) and a linear correlation was established, $k_{r,kT}^{S_1} = 0.90 \left(k_{r,SB}^{S_1}\right) - 1.59 \times 10^6$ s^1 with Pearson correlation coefficient of 0.93. A good agreement is found between the $k_r^{S_1}$ values derived from fitting eqn (2) and the Strickler–Berg analysis in cases where $\Phi_{PL} \sim 1$. However, the correspondence between values from the two methods shows

pronounced divergence for compounds that have the lowest Φ_{PL} (Table 2). This leads us to consider that the correction made for $\Phi_{PL} < 1$ is inadequate to fully account for the temperature dependence of nonradiative decay. For this reason, values for $k_r^{S_1}$ from the Strickler–Berg analysis were used to obtain correlations with the NTO overlap in the subsequent plots.

The radiative decay rate for TADF (k_r^{TADF}) for systems with fast ISC is determined principally by $k_r^{S_1}$ and ΔE_{ST}, i.e. $k_r^{TADF} = k_r^{S_1} \cdot K_{eq} = k_r^{S_1} \cdot 0.33 \exp(-\Delta E_{ST}/kT)$. It is inferred that these two parameters are closely related to the change of electron density distribution between the initial and final states in the ^{1}ICT (S_1) transition, which can be quantified by the overlap between the h-NTO and e-NTO for the emissive ^{1}ICT state. In other words, greater overlap between these NTOs will increase the oscillator strength (and $k_r^{S_1}$) as well as the ΔE_{ST} owing to an increase in the exchange energy.[53,54] Since a large $k_r^{S_1}$ and small ΔE_{ST} is preferred when aiming for a rapid k_r^{TADF}, optimizing these two conflicting effects should lead to an ideal value for the NTO overlap to achieve the fastest k_r^{TADF}. The spatial NTO overlap integral between the electron and hole associated with the electronic transitions from ground state to both S_1 and T_1 state can be computed according to the
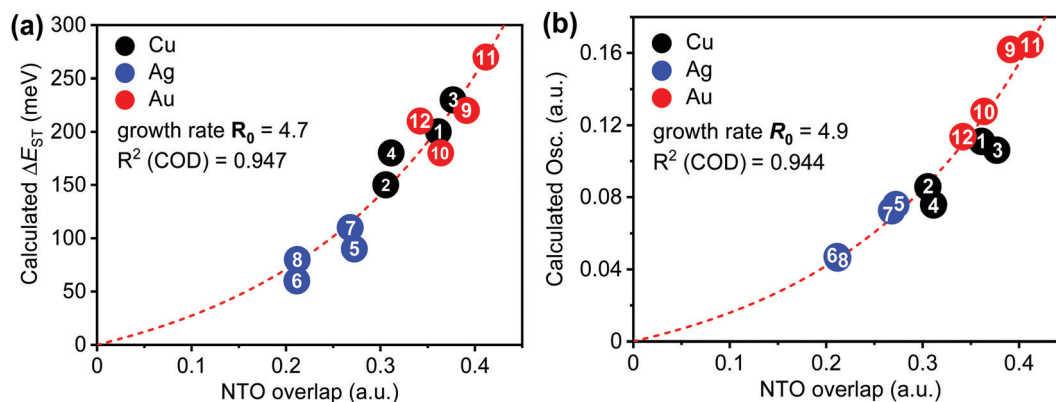
4678 | *J. Mater. Chem. C*, 2022, **10**, 4674–4683

This journal is © The Royal Society of Chemistry 2022

Fig. 5 Relationship between ^{1}ICT NTO overlap value *versus* theoretically calculated (a) ΔE_{ST} and (b) oscillator strength of the S_1 state by the TD-DFT method; fits to the data are obtained using the exponential growth function: $y = A(e^{R_0 x} - 1)$.

following expression:

$$\text{NTO overlap integral} = \frac{\sum\limits_{k} \sigma_k \int |_e^k\varphi||_h^k\varphi| d\tau}{\sum\limits_{k} \sigma_k} \quad (3)$$

where $_e^k\varphi$ and $_h^k\varphi$ are the electron and hole orbital pairs and σ_k is the amplitude of a given orbital pair that contributes to the total NTO. The overlap value was numerically evaluated as described previously.[55] Table 2 gives the NTO overlap values for the S_1 and T_1 (ICT) states, ^{1}ICT and ^{3}ICT, respectively. As observed previously,[56] the NTO overlap is larger for the triplet state than the singlet state, however the trends are the same as a function of metal, *i.e.* ^{3}ICT NTO overlaps fall in the order Au > Cu > Ag. These twelve complexes present ideal candidates to examine the dependence of $k_r^{S_1}$ and ΔE_{ST} on NTO overlap, since the different metal ions and substituents involved in the electronic transitions lead to a wide range of NTO overlap values (^{1}ICT NTO overlap from 0.21 to 0.41). The role of NTO overlap on these parameters was first investigated using values for ΔE_{ST} and oscillator strength obtained from TD-DFT calculations for the ^{1}ICT state. Plots of the two parameters *versus* ^{1}ICT NTO overlap are shown in Fig. 5a and b. It is evident that ΔE_{ST} will be zero and $k_r^{S_1}$ will be vanishingly small when

the NTO overlap is zero. Thus, these parameters were fit to the following exponential growth function: $y = A(e^{R_0 x} - 1)$, where R_0 is referred to as the growth rate. The values for both parameters obtained from TD-DFT calculations ($R_0 = 4.7$ and 4.9 for ΔE_{ST} and the oscillator strength, respectively) are proportional to the ^{1}ICT NTO overlap.

Experimental values for ΔE_{ST} and $k_{r,SB}^{S_1}$ are plotted *versus* the ^{1}ICT NTO overlap in Fig. 6. These plots can also be fit to an exponential growth function with an R_0 of 6.6 and 5.5, respectively. It is interesting to note that the exponential fits to both theoretical and experimental results give similar values. Thus, the theoretical studies and temperature dependent photophysical investigations support the hypothesis that the NTO overlap of the emissive ^{1}ICT state is indeed a key parameter controlling ΔE_{ST} and $k_r^{S_1}$, which consequently determines k_r^{TADF}.

According to the Einstein radiation law, the radiative decay rate is proportional to the cube of the emission energy. The reduced k_r^{TADF} (k_r^{TADF}/E^3, where E is the emission energy derived from the emission maximum) for complexes in this work, as well as other monometallic and bimetallic (carbene)M(*N*-carbazolyl) complexes previously reported, was plotted as a function of the NTO overlap values calculated for ^{1}ICT state (Fig. 7). Note here, only those cMa complexes that emit from

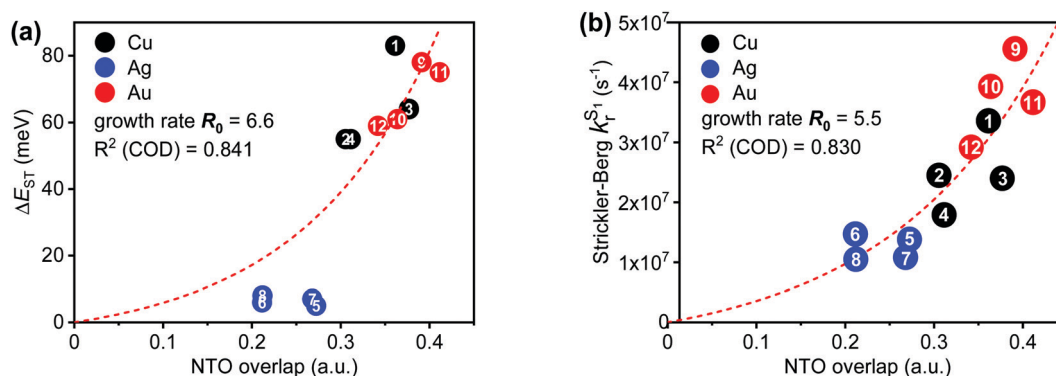Fig. 6 Relationship between ^{1}ICT NTO overlap value *versus* (a) ΔE_{ST} and (b) radiative decay rate of the ^{1}ICT state according to the Strickler−Berg equation; fits to the data are obtained from on the twelve complexes in this work using the exponential growth function: $y = A(e^{R_0 x} - 1)$.
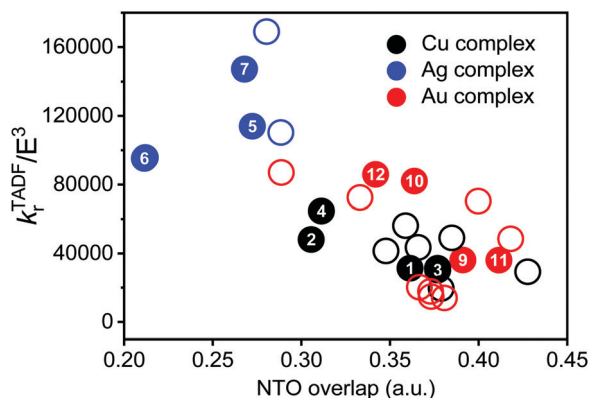
This journal is © The Royal Society of Chemistry 2022

J. Mater. Chem. C, 2022, **10**, 4674–4683 | **4679**

Fig. 7 Relationship between the reduced TADF radiative decay rate *versus* NTO overlap of the ^{1}ICT state. The closed symbols are from this work and the open symbols are for previously reported (carbene)M(carbazolyl) complexes. See the ESI† for the identities of the literature complexes.

ICT states were selected to eliminate discrepancies caused by influence from the higher lying ^{3}Cz state. From this data, rates for k_r^{TADF} are found to be fastest for complexes with NTO overlaps of 0.27–0.30 and decrease with higher and lower NTO overlap values.

A similar analysis of NTO overlap was carried out for selected organic TADF molecules to evaluate the scope of the correlations. Organic TADF molecules were chosen as listed in Table S12 (ESI†) and their photophysical properties were collected from literature.[13,49,57–77] Although the theoretical methods used to determine values for the NTO overlap were the same as those applied for the coinage metal complexes, different methods used to obtain experimental values for organic TADF molecules make the comparisons problematic. Nevertheless, the theoretical ΔE_{ST} values can still be evaluated as all compounds were calculated using the same method and basis set and show a clear increase with greater NTO overlap (Fig. 8a). It is apparent that coinage metal TADF complexes give smaller ΔE_{ST} than organic compounds with the same NTO overlap value. It is also noteworthy that for organic TADF molecules the calculated oscillator strength of the S_1 state increases significantly only when the NTO overlap is greater than 0.45 (Fig. 8b). The variation of the measured k_r^{TADF} values for organic TADF emitters as a function of NTO overlap is shown in Fig. 8c. The value for k_r^{TADF} in the organic TADF molecules also peaks at NTO overlaps of 0.2–0.3, albeit with slower rates than values found for two-coordinate coinage metal TADF complexes having comparable NTO overlaps. Thus, analysis of NTO overlaps can provide meaningful screening of organic TADF molecules for potential to have high k_{TADF} values as well.

Conclusion

In summary, a series of twelve two-coordinate Cu, Ag and Au complexes were synthesized with a cMa structure. They all display TADF emission from ICT states with fast decay lifetimes and high luminescence efficiency. NTO overlaps of the emissive ^{1}ICT states were quantified using theoretical calculations.

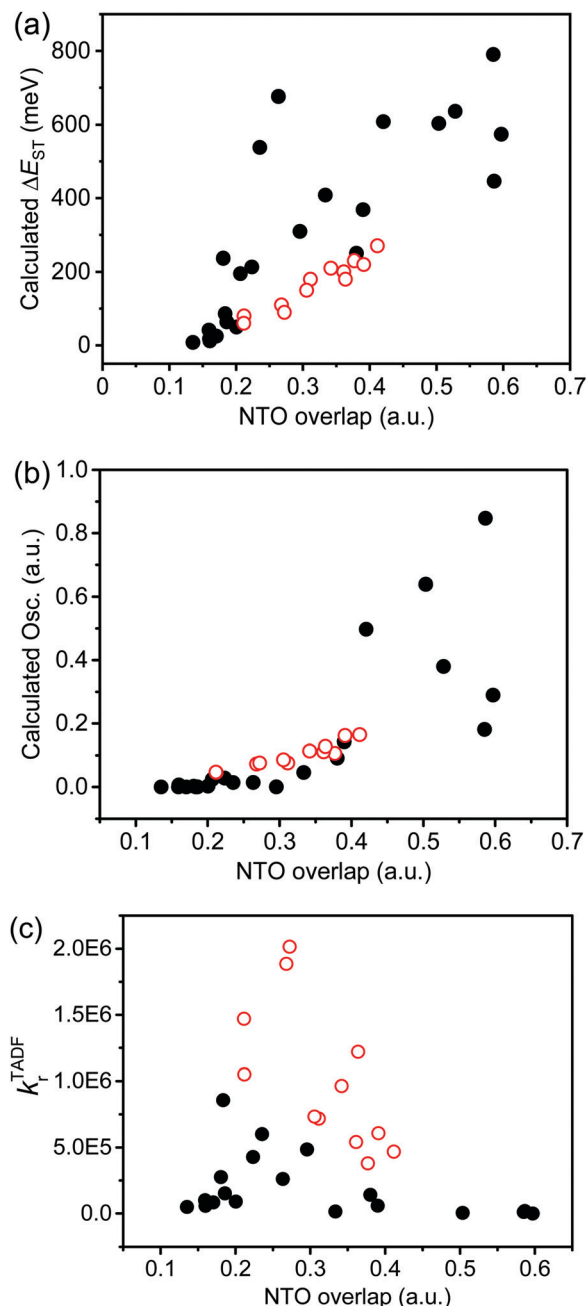Fig. 8 Relationship between NTO overlap *versus* (a) theoretically calculated ΔE_{ST}, (b) calculated S_1 state oscillator strength and (c) TADF radiative decay rate in organic TADF molecules; data of organometallic TADF complexes newly reported in this paper are shown as empty red circles.

The use of different metal ions and chemical modification on both ligands leads to NTO overlap values that cover a wide range (from 0.21 to 0.41). Detailed theoretical and experimental investigations shed light on the influence of NTO overlap on ΔE_{ST} and $k_r^{S_1}$, indicating that both parameters increase exponentially with increasing NTO overlap. However, since increasing ΔE_{ST} and k_r^{ICT} exerts opposing effects on k_r^{TADF}, the radiative rate will increase up to a maximum value with greater NTO overlap before subsequently declining. Thus, an ideal zone for

4680 | *J. Mater. Chem. C*, 2022, **10**, 4674–4683

This journal is © The Royal Society of Chemistry 2022

fast k_r^{TADF} occurs between NTO overlap values of 0.25 to 0.30. More importantly, other cMa complexes agree well with these trends, whether monometallic or bimetallic and regardless of the identity of the coinage metal ion. Thus, NTO overlap values can be used as a general method to evaluate k_r^{TADF} in such two-coordinate TADF ICT emitters. Further studies will focus on the following points: (1) examine additional cMa complexes, especially those with NTO overlap in the range from 0.1 to 0.25 to establish more accurate trends in the photophysical properties and, (2) use NTO overlap as a metric to identify molecules with a high likelihood of having fast k_r^{TADF}. This work not only provides a quantifiable metric to improve intrinsic k_r^{TADF} for two-coordinate coinage metal complexes, but also provides a new perspective to evaluate photophysical properties in other molecular systems with charge transfer excited states by using NTO overlap as a method to theoretically appraise potential candidate emitters.

Conflicts of interest

Acknowledgements

References

1 C. A. Parker and C. G. Hatchard, *Trans. Faraday Soc.*, 1961, **57**, 1894–1904.
2 R. Greinert, H. Staerk, A. Stier and A. Weller, *J. Biochem. Biophys. Methods*, 1979, **1**, 77–83.
3 V. Jankus, C.-J. Chiang, F. Dias and A. P. Monkman, *Adv. Mater.*, 2013, **25**, 1455–1459.
4 I. Lukomsky, V. Gottfried and S. Kimel, *J. Fluoresc.*, 1994, **4**, 49–51.
5 N. A. Borisevich, T. F. Raichyonok, A. A. Sukhodola and G. B. Tolstorozhev, *J. Fluoresc.*, 2006, **16**, 649–653.
6 Y. Zhang, K. Aslan, M. J. R. Previte and C. D. Geddes, *Appl. Phys. Lett.*, 2008, **92**, 013905.
7 B. Frederichs and H. Staerk, *Chem. Phys. Lett.*, 2008, **460**, 116–118.
8 J. C. Deaton, S. C. Switalski, D. Y. Kondakov, R. H. Young, T. D. Pawlik, D. J. Giesen, S. B. Harkins, A. J. M. Miller, S. F. Mickenberg and J. C. Peters, *J. Am. Chem. Soc.*, 2010, **132**, 9499–9508.

9 G. V. Zakharova, D. A. Zhizhimov, V. G. Avakyan, S. K. Sazonov, S. P. Gromov and A. K. Chibisov, *High Energ. Chem.*, 2014, **48**, 76–80.
10 I. S. Vinklárek, M. Scholz, R. Dědic and J. Hála, *Photochem. Photobiol. Sci.*, 2017, **16**, 507–518.
11 B. Vigante, K. Leitonas, D. Volyniuk, V. Andruleviciene, J. Simokaitiene, A. Ivanova, A. Bucinskas, J. V. Grazulevicius and P. Arsenyan, *Chem. – Eur. J.*, 2019, **25**, 3325–3336.
12 D. S. M. Ravinson and M. E. Thompson, *Mater. Horiz.*, 2020, **7**, 1210–1217.
13 Q. Zhang, B. Li, S. Huang, H. Nomura, H. Tanaka and C. Adachi, *Nat. Photonics*, 2014, **8**, 326–332.
14 T.-Y. Li, J. Wu, Z.-G. Wu, Y.-X. Zheng, J.-L. Zuo and Y. Pan, *Coord. Chem. Rev.*, 2018, **374**, 55–92.
15 A. Endo, M. Ogasawara, A. Takahashi, D. Yokoyama, Y. Kato and C. Adachi, *Adv. Mater.*, 2009, **21**, 4802–4806.
16 A. Endo, K. Sato, K. Yoshimura, T. Kai, A. Kawada, H. Miyazaki and C. Adachi, *Appl. Phys. Lett.*, 2011, **98**, 083302.
17 S. Lamansky, P. Djurovich, D. Murphy, F. Abdel-Razzaq, H.-E. Lee, C. Adachi, P. E. Burrows, S. R. Forrest and M. E. Thompson, *J. Am. Chem. Soc.*, 2001, **123**, 4304–4312.
18 Z. Yang, Z. Mao, Z. Xie, Y. Zhang, S. Liu, J. Zhao, J. Xu, Z. Chi and M. P. Aldred, *Chem. Soc. Rev.*, 2017, **46**, 915–1016.
19 H. Yersin, A. F. Rausch, R. Czerwieniec, T. Hofbeck and T. Fischer, *Coord. Chem. Rev.*, 2011, **255**, 2622–2652.
20 R. Czerwieniec, J. Yu and H. Yersin, *Inorg. Chem.*, 2011, **50**, 8293–8301.
21 M. J. Leitl, V. A. Krylova, P. I. Djurovich, M. E. Thompson and H. Yersin, *J. Am. Chem. Soc.*, 2014, **136**, 16032–16038.
22 T. Hofbeck, U. Monkowius and H. Yersin, *J. Am. Chem. Soc.*, 2015, **137**, 399–404.
23 R. Czerwieniec, M. J. Leitl, H. H. H. Homeier and H. Yersin, *Coord. Chem. Rev.*, 2016, **325**, 2–28.
24 H. Yersin, R. Czerwieniec, M. Z. Shafikov and A. F. Suleymanova, *Chemphyschem*, 2017, **18**, 3508–3535.
25 D. Di, A. S. Romanov, L. Yang, J. M. Richter, J. P. H. Rivett, S. Jones, T. H. Thomas, M. Abdi Jalebi, R. H. Friend, M. Linnolahti, M. Bochmann and D. Credgington, *Science*, 2017, **356**, 159.
26 A. S. Romanov, C. R. Becker, C. E. James, D. Di, D. Credgington, M. Linnolahti and M. Bochmann, *Chem. – Eur. J.*, 2017, **23**, 4625–4637.
27 P. J. Conaghan, S. M. Menke, A. S. Romanov, S. T. E. Jones, A. J. Pearson, E. W. Evans, M. Bochmann, N. C. Greenham and D. Credgington, *Adv. Mater.*, 2018, **30**, 1802285.
28 A. S. Romanov, L. Yang, S. T. E. Jones, D. Di, O. J. Morley, B. H. Drummond, A. P. M. Reponen, M. Linnolahti, D. Credgington and M. Bochmann, *Chem. Mater.*, 2019, **31**, 3613–3623.
29 R. Hamze, J. L. Peltier, D. Sylvinson, M. Jung, J. Cardenas, R. Haiges, M. Soleilhavoup, R. Jazzar, P. I. Djurovich, G. Bertrand and M. E. Thompson, *Science*, 2019, **363**, 601.
30 S. Shi, M. C. Jung, C. Coburn, A. Tadle, M. R. Daniel Sylvinson, P. I. Djurovich, S. R. Forrest and M. E. Thompson, *J. Am. Chem. Soc.*, 2019, **141**, 3576–3588.

31 R. Hamze, S. Shi, S. C. Kapper, D. S. Muthiah Ravinson, L. Estergreen, M.-C. Jung, A. C. Tadle, R. Haiges, P. I. Djurovich, J. L. Peltier, R. Jazzar, G. Bertrand, S. E. Bradforth and M. E. Thompson, *J. Am. Chem. Soc.*, 2019, **141**, 8616–8626.

32 A. S. Romanov, S. T. E. Jones, Q. Gu, P. J. Conaghan, B. H. Drummond, J. Feng, F. Chotard, L. Buizza, M. Foley, M. Linnolahti, D. Credgington and M. Bochmann, *Chem. Sci.*, 2020, **11**, 435–446.

33 P. J. Conaghan, C. S. B. Matthews, F. Chotard, S. T. E. Jones, N. C. Greenham, M. Bochmann, D. Credgington and A. S. Romanov, *Nat. Commun.*, 2020, **11**, 1758.

34 M. Gernert, L. Balles-Wolf, F. Kerner, U. Müller, A. Schmiedel, M. Holzapfel, C. M. Marian, J. Pflaum, C. Lambert and A. Steffen, *J. Am. Chem. Soc.*, 2020, **142**, 8897–8909.

35 A. Ying, Y.-H. Huang, C.-H. Lu, Z. Chen, W.-K. Lee, X. Zeng, T. Chen, X. Cao, C.-C. Wu, S. Gong and C. Yang, *ACS Appl. Mater. Interfaces*, 2021, **13**, 13478–13486.

36 F. Chotard, V. Sivchik, M. Linnolahti, M. Bochmann and A. S. Romanov, *Chem. Mater.*, 2020, **32**, 6114–6122.

37 A. S. Romanov, S. T. E. Jones, L. Yang, P. J. Conaghan, D. Di, M. Linnolahti, D. Credgington and M. Bochmann, *Adv. Opt. Mater.*, 2018, **6**, 1801347.

38 T.-y. Li, D. S. Muthiah Ravinson, R. Haiges, P. I. Djurovich and M. E. Thompson, *J. Am. Chem. Soc.*, 2020, **142**, 6158–6172.

39 H. M. J. Wang, C. S. Vasam, T. Y. R. Tsai, S.-H. Chen, A. H. H. Chang and I. J. B. Lin, *Organometallics*, 2005, **24**, 486–493.

40 V. W.-W. Yam, J. K.-W. Lee, C.-C. Ko and N. Zhu, *J. Am. Chem. Soc.*, 2009, **131**, 912–913.

41 M. C. Gimeno, A. Laguna and R. Visbal, *Organometallics*, 2012, **31**, 7146–7157.

42 A. Gómez-Suárez, D. J. Nelson, D. G. Thompson, D. B. Cordes, D. Graham, A. M. Z. Slawin and S. P. Nolan, *Beilstein J. Org. Chem.*, 2013, **9**, 2216–2223.

43 J. Feng, L. Yang, A. S. Romanov, J. Ratanapreechachai, A.-P. M. Reponen, S. T. E. Jones, M. Linnolahti, T. J. H. Hele, A. Köhler, H. Bässler, M. Bochmann and D. Credgington, *Adv. Funct. Mater.*, 2020, **30**, 1908715.

44 C. R. Hall, A. S. Romanov, M. Bochmann and S. R. Meech, *J. Phys. Chem. Lett.*, 2018, **9**, 5873–5876.

45 J. Feng, A.-P. M. Reponen, A. S. Romanov, M. Linnolahti, M. Bochmann, N. C. Greenham, T. Penfold and D. Credgington, *Adv. Funct. Mater.*, 2021, **31**, 2005438.

46 S. Thompson, J. Eng and T. J. Penfold, *J. Chem. Phys.*, 2018, **149**, 014304.

47 E. J. Taffet, Y. Olivier, F. Lam, D. Beljonne and G. D. Scholes, *J. Phys. Chem. Lett.*, 2018, **9**, 1620–1626.

48 T.-y. Li, D. G. Shlian, P. I. Djurovich and M. E. Thompson, *Chem. – Eur. J.*, 2021, **27**, 6191–6197.

49 Y. Tsuchiya, S. Diesing, F. Bencheikh, Y. Wada, P. L. dos Santos, H. Kaji, E. Zysman-Colman, I. D. W. Samuel and C. Adachi, *J. Phys. Chem. A*, 2021, **125**, 8074–8089.

50 T. Chen, L. Zheng, J. Yuan, Z. An, R. Chen, Y. Tao, H. Li, X. Xie and W. Huang, *Sci. Rep.*, 2015, **5**, 10923.

51 C. Zhang, F. Zhang, S. Lv, M. Shi and J. Zhang, *New J. Chem.*, 2017, **41**, 1889–1892.

52 S. J. Strickler and R. A. Berg, *J. Chem. Phys.*, 1962, **37**, 814–822.

53 J. N. Turro, V. Ramamurthy, J. C. Scaiano, *Principles of Molecular Photochemistry: An Introduction*, 2009, University Science Book, Sausalito, California.

54 S. P. McGlynn, T. Azumi and M. Kinoshita, *Molecular Spectroscopy of the Triplet State*, 1969, Prentice-Hall, Inc., Englewood Cliffs, New Jersey.

55 A. C. Tadle, K. A. El Roz, C. H. Soh, D. Sylvinson Muthiah Ravinson, P. I. Djurovich, S. R. Forrest and M. E. Thompson, *Adv. Funct. Mater.*, 2021, **31**, 2101175.

56 T. Chen, L. Zheng, J. Yuan, Z. An, R. Chen, Y. Tao, H. Li, X. Xie and W. Huang, *Sci. Rep.*, 2015, **5**, 10923.

57 H. Tanaka, K. Shizu, H. Miyazaki and C. Adachi, *Chem. Commun.*, 2012, **48**, 11392–11394.

58 Y. Liu, C. Li, Z. Ren, S. Yan and M. R. Bryce, *Nat. Rev. Mater.*, 2018, **3**, 18020.

59 M. Godumala, S. Choi, M. J. Cho and D. H. Choi, *J. Mater. Chem. C*, 2019, **7**, 2172–2198.

60 H. Noda, X.-K. Chen, H. Nakanotani, T. Hosokai, M. Miyajima, N. Notsuka, Y. Kashima, J.-L. Brédas and C. Adachi, *Nat. Mater.*, 2019, **18**, 1084–1090.

61 H. Noda, H. Nakanotani and C. Adachi, *Sci. Adv.*, 2018, **4**, 6910.

62 L.-S. Cui, A. J. Gillett, S.-F. Zhang, H. Ye, Y. Liu, X.-K. Chen, Z.-S. Lin, E. W. Evans, W. K. Myers, T. K. Ronson, H. Nakanotani, S. Reineke, J.-L. Bredas, C. Adachi and R. H. Friend, *Nat. Photonics*, 2020, **14**, 636–642.

63 Y. Kondo, K. Yoshiura, S. Kitera, H. Nishi, S. Oda, H. Gotoh, Y. Sasada, M. Yanai and T. Hatakeyama, *Nat. Photonics*, 2019, **13**, 678–682.

64 J. U. Kim, I. S. Park, C.-Y. Chan, M. Tanaka, Y. Tsuchiya, H. Nakanotani and C. Adachi, *Nat. Commun.*, 2020, **11**, 1765.

65 N. Aizawa, Y. Harabuchi, S. Maeda and Y.-J. Pu, *Nat. Commun.*, 2020, **11**, 3909.

66 D. Hall, S. M. Suresh, P. L. dos Santos, E. Duda, S. Bagnich, A. Pershin, P. Rajamalli, D. B. Cordes, A. M. Z. Slawin, D. Beljonne, A. Köhler, I. D. W. Samuel, Y. Olivier and E. Zysman-Colman, *Adv. Opt. Mater.*, 2020, **8**, 1901627.

67 J. Lee, N. Aizawa and T. Yasuda, *Chem. Mater.*, 2017, **29**, 8012–8020.

68 S. Jeong, Y. Lee, J. K. Kim, D.-J. Jang and J.-I. Hong, *J. Mater. Chem. C*, 2018, **6**, 9049–9054.

69 I. S. Park, K. Matsuo, N. Aizawa and T. Yasuda, *Adv. Funct. Mater.*, 2018, **28**, 1802031.

70 S. Wang, X. Yan, Z. Cheng, H. Zhang, Y. Liu and Y. Wang, *Angew. Chem., Int. Ed.*, 2015, **54**, 13068–13072.

71 K. Shizu, H. Noda, H. Tanaka, M. Taneda, M. Uejima, T. Sato, K. Tanaka, H. Kaji and C. Adachi, *J. Phys. Chem. C*, 2015, **119**, 26283–26289.

72 S. Hirata, Y. Sakai, K. Masui, H. Tanaka, S. Y. Lee, H. Nomura, N. Nakamura, M. Yasumatsu, H. Nakanotani, Q. Zhang, K. Shizu, H. Miyazaki and C. Adachi, *Nat. Mater.*, 2015, **14**, 330–336.

73 T. Hatakeyama, K. Shiren, K. Nakajima, S. Nomura, S. Nakatsuka, K. Kinoshita, J. Ni, Y. Ono and T. Ikuta, *Adv. Mater.*, 2016, **28**, 2777–2781.

74 T.-A. Lin, T. Chatterjee, W.-L. Tsai, W.-K. Lee, M.-J. Wu, M. Jiao, K.-C. Pan, C.-L. Yi, C.-L. Chung, K.-T. Wong and C.-C. Wu, *Adv. Mater.*, 2016, **28**, 6976–6983.

75 Q. Zhang, D. Tsang, H. Kuwabara, Y. Hatae, B. Li, T. Takahashi, S. Y. Lee, T. Yasuda and C. Adachi, *Adv. Mater.*, 2015, **27**, 2096–2100.

76 J. Guo, X.-L. Li, H. Nie, W. Luo, S. Gan, S. Hu, R. Hu, A. Qin, Z. Zhao, S.-J. Su and B. Z. Tang, *Adv. Funct. Mater.*, 2017, **27**, 1606458.

77 G. Xie, X. Li, D. Chen, Z. Wang, X. Cai, D. Chen, Y. Li, K. Liu, Y. Cao and S.-J. Su, *Adv. Mater.*, 2016, **28**, 181–187.